Structural and Multidisciplinary Optimization (2024) 67:141
https://doi.org/10.1007/s00158-024-03849-0

RESEARCH PAPER

Topology optimization for fatigue reserve factors

Roman Sartorti[1] · **Benedikt Kriegesmann**[2] · **David Hawla**[4] · **Claus B. W. Pedersen**[3]

Received: 26 February 2024 / Revised: 10 June 2024 / Accepted: 10 July 2024 / Published online: 7 August 2024

Abstract
This paper describes a topology optimization approach that applies the common fatigue analysis practices of rainflow cycle counting and critical plane searches to cover both proportional and non-proportional fatigue loading conditions of metals. The existing literature on topology optimization has so far mainly considered fatigue damage under proportional loading conditions and typically uses continuous damage models to avoid the discontinuous nature of fatigue rainflow cycle counting and critical plane searches. Furthermore, previous publications often introduced heuristic schemes to scale the fatigue damage and set the move limits for the design variables rather low to avoid oscillations in the design variables and damage responses during the optimization iterations, because fatigue damage is typically highly localized. Therefore, these approaches cause many optimization iterations. Contrarily, our present approach applies the fatigue reserve factor (*FRF*) directly in the optimization formulation instead of the fatigue damage where *FRF* is a fatigue reserve factor for infinite fatigue life. The inverse *FRF* scales nearly linearly with the stresses. Therefore, the present approach needs no heuristic scaling for the fatigue topology optimization. The numerical implementation applies the semi-analytic adjoint sensitivity method for multiple load cases. Numerically, *FRF* shows more stable optimization convergence using less optimization iterations. Different *FRF* topology-optimized designs for a variety of fatigue damage types are validated and compared. Additionally, the optimized *FRF* designs are compared to both strictly stiffness optimized designs and stress strength optimized designs.

Keywords Fatigue reserve factor · Strength optimization · Topology optimization · Semi-analytic adjoint sensitivities

1 Introduction

Fatigue damage responses in topology optimization for structural strength optimization has several numerical and theoretical challenges. Therefore, it is not widely applied in topology optimization even though fatigue damage validation and certification are typical critical sign-off criteria for many practical structural applications. The first challenge is that fatigue damage is a very local measure at the material points creating many constraints if no aggregation function or similar approaches are applied for constructing a single constraint (Le et al. 2010; Verbart et al. 2016; Norato et al. 2022; Bruggi 2008). Secondly, it is challenging to apply adjoint sensitivities for realistic fatigue modeling including non-proportional loading and rainflow counting for the time histories in conjunction with practical plane search supporting different fatigue damage parameter types depending upon the specific material characteristics (Sartorti et al. 2023). Thirdly, as the fatigue damage responses frequently change by several magnitudes over a few optimization iterations as well as the locations of the fatigue damage hotspots change significantly during the optimization iterations then the fatigue damage topology optimization convergence yields many optimization iterations and, therefore, high computational costs. In the present work, we suggest novel contributions addressing the second and third issue with respect to infinite life fatigue topology optimization.

Responsible editor: W. H. Zhang

✉ Roman Sartorti
roman.sartorti@tuhh.de

[1] Institute for Ship Structural Design and Analysis, Hamburg University of Technology, Am Schwarzenberg-Campus 4C, 21073 Hamburg, Germany

[2] Institute for Structural Mechanics in Lightweight Design, Hamburg University of Technology, Eissendorfer Strasse 40, 21073 Hamburg, Germany

[3] Dassault Systèmes Deutschland GmbH, Glockengiesserwall 22, 20095 Hamburg, Germany

[4] Dassault Systèmes, Atwood Ave 1301, Johnston, RI 02919, USA

Initial work on fatigue topology optimization (Holmberg et al. 2013) converts the fatigue constraints into stress constraints. Prior to the optimization, a fatigue analysis is performed to find the maximum allowable stress corresponding to the fatigue constraint for a given proportional load history. Afterward, the first principal stress criterion is applied as stress constraint for the topology optimization. However, this approach (Sartorti et al. 2023) is not feasible for several load histories and non-proportional loading, and hence, would yield non-optimal designs for realistic fatigue topology optimization. The work by Jeong et al. (2015) includes fatigue damage directly in the topology optimization workflow using a signed von Mises stress-life method. The stresses are calculated for static and harmonic finite element procedures. A characteristic is that the non-differentiability of the mean stress corrections is replaced by smooth approximations under the assumption of proportional mechanical loads. The work in Oest and Lund (2017) and Olesen et al. (2021) proposes a more general topology optimization method for fatigue damage optimization, including rainflow counting. However, the rainflow counting is performed on load histories assuming proportional loading. A Sines stress-life damage parameter is applied in Oest and Lund (2017), while (Olesen et al. 2021) applies the principal stress-life damage parameter for the fatigue calculation using a transversely isotropic material. Furthermore, Zhang et al. (2019) proposes an approach for realistic non-proportional load scenarios considering signed von Mises as damage parameter and rainflow counting of the stress history. This leads to higher computational costs since the rainflow counting is performed for every material point. To avoid rainflow counting (Suresh et al. 2022, 2021, 2020) proposes a continuous damage accumulation approach in time which also supports non-proportional loading. However, this approach causes increased computational costs as the stress time histories are calculated explicitly which is impractical for realistic load histories. Therefore, Suresh et al. (2022) later suggested an approximate continuous damage accumulation approach using extrapolation. However, the extrapolation causes a lack of accuracy and the reduction in computational costs is not significant. In contrast to the above-mentioned references, we resolve the second issue and do support fatigue topology optimization for many different fatigue damage types, including critical plane for non-proportional loading, and therefore provides a more general approach for many practical applications (Lee et al. 2012).

As an additional motivation then the work in Slebioda et al. (2023) recently presented a fatigue optimization framework applying the signed von Mises method for the fatigue analysis. Therein, the authors emphasize the necessity of including other fatigue damage criteria, including critical plane fatigue analysis, which is addressed in the present approach.

Furthermore, the present work addresses the third issue that the number of optimization iteration is frequently high as the highly non-linear fatigue damage dependency on the stresses causes the optimization to require small design changes per optimization iteration for avoiding convergence issues. To circumvent the convergence issues, Oest and Lund (2017) suggests a logarithm function on the aggregated damage constraint, Zhang et al. (2019) suggests scaling the damage using the Basquin factor, and Olesen et al. (2021) applies a modified aggregation function using the Basquin scaling factor and combining an ordinary p-mean function having an inverse p-mean function. The heuristic scaling schemes reduce the fatigue damage non-linearity and decrease the number of required optimization iterations. However, none of the suggested scaling methods works properly for all general sensitivity-based topology optimization formulations that include fatigue damage, and additionally, they require heuristic parameters that must be chosen specifically for each given fatigue topology optimization application. Instead of applying these kinds of scaling factors for the fatigue topology optimization then we explore the fatigue reserve safety factors (*FRF*s) for infinite fatigue life topology optimization.

The rest of the paper is structured as follows. Section 2 explains the motivation for using fatigue reserve safety factors (*FRF*s) for fatigue topology optimization addressing how to formulate a well-posed fatigue topology optimization. After summarizing the underlying theory in Sects. 3, 4 extends the previous work of Sartorti et al. (2023) for adjoint semi-analytical fatigue sensitivities to support *FRF*s in topology optimization and to include a stress relaxation scheme similar to Bruggi (2008) and Holmberg et al. (2013) for strength topology optimization. Section 5 outlines the numerical implementation and Sect. 6 shows several numerical experiments including crossover checks for the different fatigue damage parameter types.

2 Motivation

Including fatigue topology optimization for real industrial applications has practical challenges.

First, several different fatigue damage parameters can be applied, i.e., the sensitivities need to be derived explicitly for each damage parameter type. We avoid this by applying semi-analytic sensitivities using a finite differences scheme for the partial derivatives of the fatigue calculation at the material points also supporting multiaxial loading scenarios.

Secondly, the number of optimization iterations is typically large, see Figure 1. This is due to the highly non-linear fatigue response and the local characteristic of fatigue damage. Thus, the change of the design variables during one optimization iteration has to be small

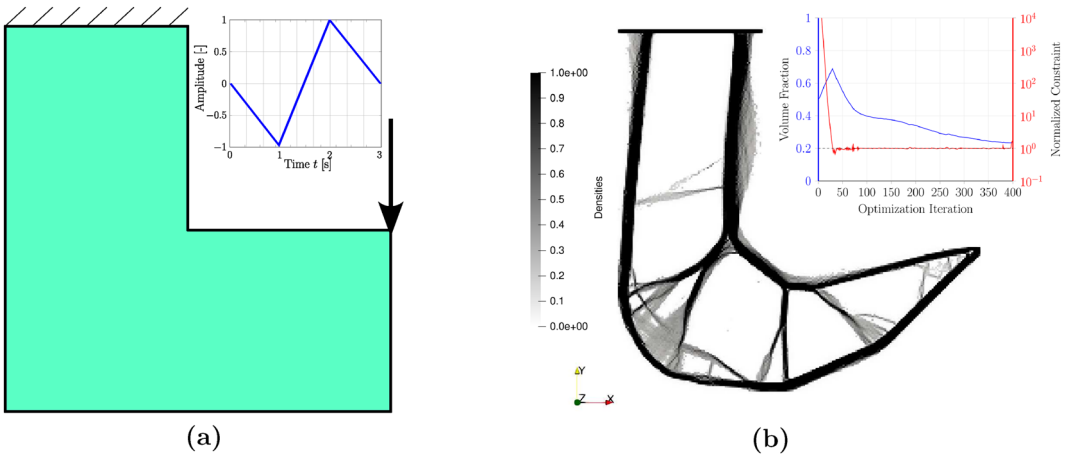

Fig. 1 Topology optimization of the L-bracket example subject to one load case. **a** Geometry and load histories applying the von Mises stress damage parameter. **b** The relative density distribution after 400 optimization iterations and the corresponding optimization iteration history. The initial design is highly infeasible and the fatigue damage constraint changes by orders of magnitude in the first optimization iterations

to avoid oscillations of the critical hot spots between the optimization iterations. If the design changes are too large in the first optimization iterations then the fatigue values can easily change by orders of magnitude. To address this issue then the previous referenced work scales the fatigue damage using different methods, e.g., using log function (Oest and Lund 2017), inverse p-mean scaling (Zhang et al. 2019) or the so-called Basquin scaling (Olesen et al. 2021). However, none of these methods are well suited for arbitrary fatigue topology optimization formulations.

Therefore, in the present work, we suggest to apply the fatigue reserve factor (*FRF*) to suppress the non-linearity.

Thirdly, a fatigue topology optimization formulation can easily be articulated as an ill-posed optimization problem since the fatigue damage for common materials is only modeled in the tensile direction. This is analogous to optimization formulations where principal stresses are considered as the parts being under pure compression do not see any critical stresses or damage. Thus, additional constraints are required to both ensure stable convergence and a well-posed optimization formulation.

Hence, Olesen et al. (2021) and Suresh et al. (2022) state that an additional constraints addressing stiffness or von Mises stress have to be added to ensure a well-posed topology optimization formulation.

In our previous work (Sartorti et al. 2023), we presented a method to incorporate arbitrary damage parameter types such as Brown-Miller, normal stress, normal strain, and von Mises stress for non-parametric sizing, shape, and bead design variables. These types of design variable optimizations ensure an inherent stiffness for the optimization problem so no additional stiffness requirements need to be added to the fatigue optimization formulation. Hence, topology optimization was not addressed in this (Sartorti et al. 2023).

As an alternative to the previous approaches, we propose to incorporate fatigue into the topology optimization using an infinite life fatigue analysis. Hence, we apply the inverse *FRF* because this has the appealing advantage that it scales almost linearly with the stresses, i.e., no additional non-linearity is introduced for the optimization compared to directly applying fatigue damage in the topology optimization formulation.

3 Theory

3.1 Fatigue analysis

Designing reliable products often requires to predict when and where high cycle fatigue failures occur. Overall, fatigue analysis can be differentiated into two major classes:

- Finite fatigue life analysis predicts the damage occurring in the material for a certain cyclic loading history. Some finite life methods predict the crack angle using critical plane analysis (Meggiolaro et al. 2015). This fatigue classification can further be subdivided into two categories:
  - High Cycle Fatigue (HCF): mainly driven by stresses being below the cyclic yield stress.
  - Low Cycle Fatigue (LCF): mainly driven by elasto-plastic deformations induced by stresses at and over the yield stress.
- Infinite fatigue life analysis predicts how close the actual fatigue loading is to the endurance limit. Similar to the

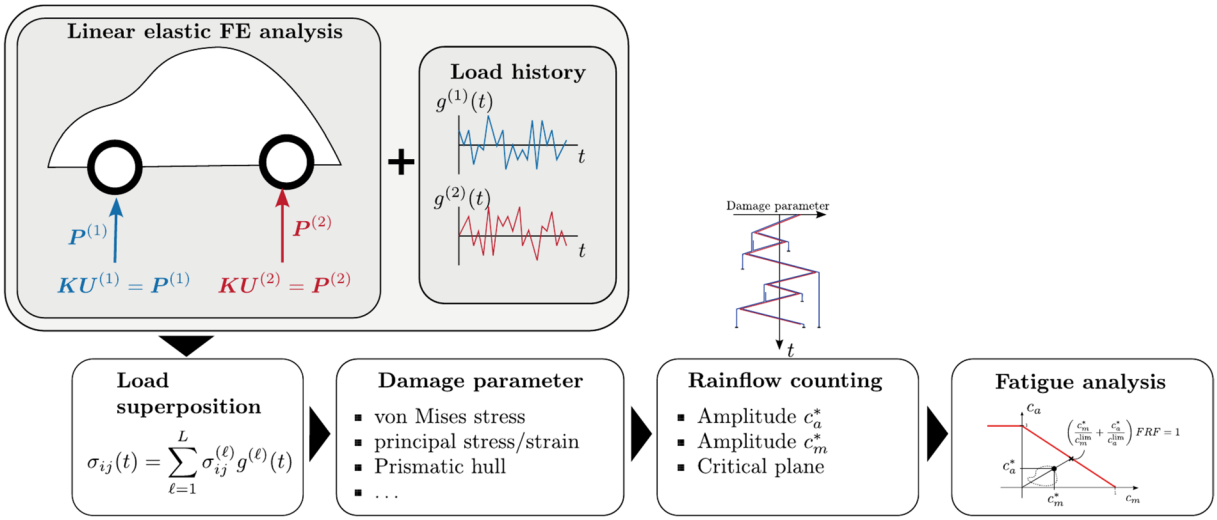

Fig. 2 Flowchart of a fatigue analysis for the fatigue reserve factor (*FRF*). The stresses obtained from multiple linear elastic load cases are superimposed using the load histories to obtain the stress history in time. The stresses in time calculate the value of a specified damage parameter type. Afterward, the amplitude and mean values of the damage parameters are calculated using a rainflow counting algorithm. Lastly, the fatigue analysis for *FRF* is determined based on the values obtained from the rainflow counting

finite life analysis, different fatigue parameter types can be applied for different material characteristics.

In the present work, we propose to use an infinite life measure to incorporate fatigue requirements into topology optimization. In contrast to finite life analysis, no additional scaling is required to reduce the non-linearity. More details are given in the following section.

3.2 Fatigue reserve factors

A fatigue reserve factor (*FRF*) is a special definition of an infinite life safety factor in fatigue. We use the *FRF* term rather than other safety factor types since *FRF* determines the most damaging fatigue cycle in the stress history of a material point being fundamentally different to using relatively simple equations for the mean stress-dependent fatigue limit. One of the simplest fatigue reserve factors uses the Goodman mean stress correction, see Fig. 3, for which one of the most practical applied measures is defined as

$$\left(\frac{\sigma_a^*}{\sigma_{-1}} + \frac{\sigma_m^*}{\sigma_\mathrm{u}}\right) FRF = 1, \tag{1}$$

where σ_u and σ_{-1} are the ultimate tensile strength and the fatigue limit for a fully reversed loading, respectively. This scales the entire load history, i.e., both stress amplitudes and mean stresses equally. These *FRF* values are inversely proportional to the stresses, whereas a $1/FRF$ parameter is linearly proportional to the stresses. Hence, Eq. (1) is rewritten as

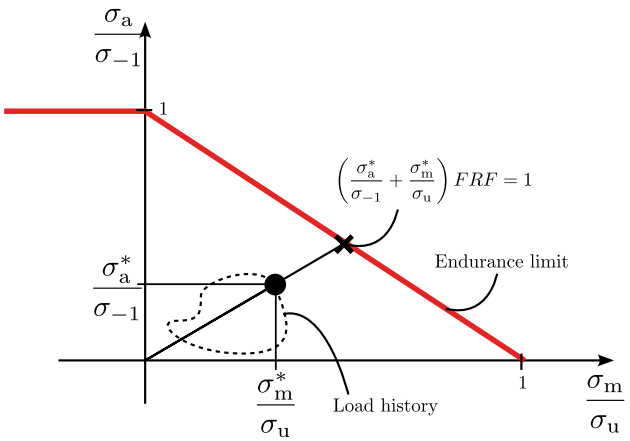

Fig. 3 Visualization of the Goodman mean stress correction and the relation to the *FRF* calculation defined in Eq. (1)

$$\frac{1}{FRF} = \frac{\sigma_a^*}{\sigma_{-1}} + \frac{\sigma_m^*}{\sigma_u}. \tag{2}$$

To compute the stress amplitudes and mean stresses, various methods are used to convert the stress tensor history into the scalar measures σ_a^* and σ_m^*. One of the most common methods for ductile materials applies the von Mises equivalent stress amplitudes and mean stresses. For brittle materials, the most common method applies the principal stress amplitudes (Stephens and Fuchs 2001).

These methods work fine for proportional loading where the fatigue cycles are determined in closed form. Determining the cycles when the local stress tensor histories exhibit

non-proportional loading are more challenging and several contributions have been developed, e.g., rainflow counting (Rychlik 1996; ASTM 2017), various critical plane methods (Stephens and Fuchs 2001; Meggiolaro et al. 2015), the Dang Van method (Socie 2000; Karolczuk et al. 2016; Slebioda et al. 2023), and the prismatic hull method (Mamiya et al. 2009). Figure 2 shows that the non-proportional loading histories increase the computational costs for the *FRF* calculation as the rainflow counting and the critical plane analysis are often included compared to the methods, which can be applied for proportional loading.

3.3 Topology optimization formulation

The optimization is defined by the objective function g_0 and I constraints, $g_i$which can be constrained by an upper constraint value g_i^{U} and a lower constraint value g_i^{L}, respectively. The functions g_0 and g_i are also referred to as design responses and are functions of the topology optimization design variables $\boldsymbol{\varphi}$. Typically, a regularization scheme is applied to obtain the physical topology design variables $\bar{\varphi}_j \in \bar{\boldsymbol{\varphi}}(\boldsymbol{\varphi})$ being a function of the topology design variables $\boldsymbol{\varphi}$ (Sigmund and Maute 2013). The physical design variables are obtained using a filter as regularization. Hence, the filter both suppresses checkerboarding and introduces a minimum length scale. We apply the well-known density filter (Sigmund and Maute 2013) for this purpose, given as

$$\begin{aligned} \bar{\varphi}_j &= \frac{\sum_{i=1}^{N_n} w_i \varphi_i}{\sum_{i=1}^{N_n} w_i}, \\ w_i &= \min(R^2 - \|\boldsymbol{x}_j^c - \boldsymbol{x}_i^c\|^2, 0) \end{aligned} \quad , \tag{3}$$

where R is the filter radius and $\boldsymbol{x}_j^c$ is the centroid of element j.

The design variables $\boldsymbol{\varphi}$ are restricted by an upper bound φ_j^{U} and a lower bound φ_j^{L} where $j = 1, 2, \ldots, J$ and J is the total number of design variables. The lower bound is set to zero ($\boldsymbol{\varphi}^{\mathrm{L}} = 0$) representing the void material and the upper bound is set to 1 ($\boldsymbol{\varphi}^{\mathrm{U}} = 1$) representing the solid material (Bendsøe and Sigmund 2007). Moreover, the structural equilibrium has to be fulfilled for all load cases and, hence, the residual $\boldsymbol{R}^{(\ell)}$ is zero for all load cases L. The stiffness matrix $\boldsymbol{K}$ and the displacement field $\boldsymbol{u}^{(\ell)}$ depend on the physical design variables $\bar{\boldsymbol{\varphi}}$. Therefore, the optimization is formulated as

$$\min_{\boldsymbol{\varphi}} g_0(\boldsymbol{\varphi}) \quad , \tag{4}$$

$$\text{s.t.} g_i^{\mathrm{L}} \leq g_i(\boldsymbol{\varphi}) \leq g_i^{\mathrm{U}}, \quad \text{with } i = 1, \ldots, I, \tag{5}$$

$$\varphi_j^{\mathrm{L}} \leq \varphi_j \leq \varphi_j^{\mathrm{U}}, \quad \text{with } j = 1, \ldots, J, \tag{6}$$

$$\boldsymbol{K}(\bar{\boldsymbol{\varphi}})\boldsymbol{u}^{(\ell)}(\bar{\boldsymbol{\varphi}}) = \boldsymbol{P}^{(\ell)}, \quad \text{with } \ell = 1, \ldots, L. \tag{7}$$

To solve Eqs. (4)–(7), a sensitivity-based optimization algorithm is applied using mathematical programming in the form of the method of moving asymptotes (MMA) (Svanberg 2002, 1987, 2007). The structural sensitivities w.r.t the design variables $\boldsymbol{\varphi}$ are calculated using the adjoint method as shown in the following.

3.4 Inverse *FRF*

The fatigue reserve factor (*FRF*) introduced in Sect. 3.2 has *FRF* values ranging from 0 to infinity *FRF* for none failing strength fatigue designs. This is disadvantageous when the *FRF* is applied either as objective function in Eq. (4) or as a constraint in Eq. (5). The work in Ref. (Svanberg 1987, 2002, 2007) for mathematical programming methods using moving asymptotes recommends that reasonable values for both the objective function and the constraints should be less than 100. Therefore, we introduce the fatigue measure F_k being the design response for the inverse of the *FRF* at each integration point k as follows:

$$F_k = \frac{1}{FRF_k}. \tag{8}$$

Additionally, various numerical experiments showed that the number of optimization iterations is significantly reduced when minimizing the inverse *FRF* as opposed to maximizing the *FRF* as an objective function or constraining the inverse *FRF* as opposed to directly constraining *FRF*. Additionally, for moderate to high move limits for the design variables, the optimization formulation using the inverse *FRF* still converges smoothly, whereas the optimization formulation directly using the *FRF* frequently oscillates significantly during the optimization iterations or diverges. Furthermore, this observation is theoretically supported by Eq. (2) where the inverse *FRF* scales linearly with the stress tensor.

In the following sections, we derive the sensitivities of F being the inverse *FRF*.

4 Adjoint sensitivities for inverse fatigue reserve factor

4.1 Structural equilibrium

The structural model is analyzed using linear finite element (Zienkiewicz and Taylor 2005) (FE) modeling, see Fig. 2. All examples are considered to be linear static. Hence,

the model is described by the following linear system of equations

$$\boldsymbol{K}\boldsymbol{u}^{(\ell)} = \boldsymbol{P}^{(\ell)}., \tag{9}$$

where $\boldsymbol{K}$ is the stiffness matrix, $\boldsymbol{u}^{(\ell)}$ are the displacements and $\boldsymbol{P}^{(\ell)}$ describes the external loads for all load cases $\ell = 1, \dots, L$. Since the system is linear, the factorized stiffness matrix can be applied for all load cases where only the right-hand side for the external load is substituted.

In order to determine the fatigue damage, the stress tensors $\sigma_{ij_k}^{(\ell)}$ are calculated for each load case ℓ at material point k. Those are derived using the strain displacement matrix $\mathbf{B}$ and the constitutive material matrix $\mathbb{C}$ being a function of the Young's modulus. Thus, the stress tensor $\sigma_{ij_k}^{(\ell)}$ at each material point k for load case ℓ is calculated as

$$\bar{\sigma}_{ij_k}^{(\ell)} = \mathbb{C}\mathbf{B}\boldsymbol{u}_k^{(\ell)}, \tag{10}$$

where $\boldsymbol{u}_k^{(\ell)}$ are the displacements evaluated at material point k.

4.2 Material interpolation and stress relaxation

In the present work, the well-known solid isotropic material interpolation using penalization (SIMP) (Bendsøe and Sigmund 2007) for the material stiffness is applied. Thus, the material interpolation for the SIMP approach of the Young's modulus $E(\bar{\varphi}_e(\varphi))$ for each finite element e reads

$$E(\bar{\varphi}_e(\varphi)) = E_{\text{void}} + \bar{\varphi}_e(\boldsymbol{\varphi})^p E_{\text{solid}}, \tag{11}$$

where $E_{\text{void}} = 10^{-9}$ is introduced to avoid singularity of the stiffness matrix and E_{solid} represents the Young's modulus of the solid material $\varphi = 1$. The material penalty p is set to $p = 3$ for all examples in the present work.

We use a stress relaxation for the stresses in Eq. (10) to avoid singularities in strength-based topology optimization as

$$\sigma_{ij}(\bar{\varphi}_e(\boldsymbol{\varphi})) = \bar{\varphi}_e(\boldsymbol{\varphi})^{p-q}\bar{\sigma}_{ij} \tag{12}$$

fulfilling the condition $p > q$. Therefore, the stresses vanish for void elements when the design variables approach the lower bound for the design variables (Bruggi 2008; Holmberg et al. 2013) and at solid material points, the stress values are unrelaxed. For all present examples, $q = 2.5$ is applied.

4.3 Fatigue sensitivity analysis

Similarly to Sartorti et al. (2023), we apply semi-analytical adjoint sensitivities for the multiaxial fatigue design responses. The fatigue measure F_k at material point k depends on the stress tensors of all load cases, i.e.,

$$F_k(\sigma_{ij_k}^{(\ell)}(\boldsymbol{\varphi}, \boldsymbol{u}_k^{(\ell)}(\boldsymbol{\varphi}))) \tag{13}$$

and is not directly influenced by the design variable φ. To obtain a single design response for the local F_k values, we apply an aggregation scheme similar to stress-based topology optimizations formulations. Herein, we use the p-mean norm as aggregation function Ψ_F to obtain a single design response over the fatigue measure for all material points k as follows:

$$\Psi_F = c\left(\frac{1}{K}\sum_{k=1}^{K}\left(F_k\right)^Q\right)^{\frac{1}{Q}}. \tag{14}$$

The p-mean norm approach does not accurately approximate the maximum stress value when using, e.g, $Q = 6$. This approximation issue also persists for higher Q-values. Therefore, we apply an adaptive scaling method as suggested in Le et al. (2010), Oest and Lund (2017), and Zhang et al. (2019) which ensures that the true maximum fatigue measure of the optimized design fulfills the applied fatigue constraint by adaptively adjusting the scaling factor c. Numerical experiments show that a too high value of Q causes numerical instabilities and a low value of Q causes an erroneous approximation of the maximum fatigue measure and the corresponding adjoint fatigue sensitivities. Setting $Q = 6$ proves to be numerical stable and causes only a small error in the approximation of Eq. (14) which is observed by reasonable values for c. Therefore, all examples in the present work apply $Q = 6$ for Eq. (14).

Then the semi-analytic adjoint sensitivities are derived for the present aggregated fatigue design response Ψ_F using the adjoint sensitivity approach in Sartorti et al. (2023) for fatigue damage, as follows:

$$\begin{aligned}\frac{\mathrm{d}\Psi_F}{\mathrm{d}\boldsymbol{\varphi}} = \sum_{\ell=1}^{L}\Bigg[\sum_{k=1}^{K}\left(\frac{\partial\Psi_F}{\partial F_k}\frac{\partial F_k}{\partial\sigma_{ij_k}^{(\ell)}}\frac{\partial\sigma_{ij_k}^{(\ell)}}{\partial\boldsymbol{\varphi}}\right)\\ +\boldsymbol{\lambda}^{(\ell)\top}\frac{\partial\boldsymbol{K}}{\partial\boldsymbol{\varphi}}\boldsymbol{u}^{(\ell)}\Bigg]\end{aligned} \tag{15}$$

and the adjoint system determining the Lagrange multiplier $\boldsymbol{\lambda}^{(\ell)}$ per load case yields

$$\begin{aligned}\boldsymbol{K}\boldsymbol{\lambda}^{(\ell)} = -\left(\sum_{k=1}^{K}\frac{\partial\Psi_F}{\partial F_k}\frac{\partial F_k}{\partial\sigma_{ij_k}^{(\ell)}}\frac{\partial\sigma_{ij_k}^{(\ell)}}{\partial\boldsymbol{u}^{(\ell)}}\right)^{\top}.\\ \text{where } \ell = 1, 2, \dots, L.\end{aligned} \tag{16}$$

The following section describes in detail how the partial derivatives for the inverse FRF ($F = 1/FRF$) are calculated using semi-analytical adjoint finite difference.

4.3.1 Partial derivative of inverse *FRF*

The partial derivative of the inverse *FRF* w.r.t the stress tensor for Eqs. (16) and (17) yields the following using numerical finite difference

$$\frac{\partial F_k}{\partial \sigma_{ij_k}} = -\frac{1}{FRF_k{}^2}\frac{\partial FRF_k}{\partial \sigma_{ij_k}} \approx -\frac{1}{FRF_k{}^2}\frac{\Delta FRF_k}{\Delta \sigma_{ij_k}}. \tag{17}$$

The finite difference approximations are calculated per material point k. Hence, there is no coupling between material points for the evaluations of FRF_k. A total of three and six finite difference function calls for the fatigue calculation is required per material point as the stress tensor has three and six components in 2D and 3D, respectively. Thus, the partial finite difference for the semi-analytical adjoint sensitivities has low computational costs and at the same time generally supports many different damage parameter types, including critical plane methods. Throughout various numerical experiments, we find that a stress variation of $\Delta\sigma = 0.001 \cdot 0.005 \cdot |\max \sigma_{ij_k}^{(\ell)}|$ works well and has similarly being verified in Sartorti et al. (2023) for shape, sizing, and bead optimization where $|\max \sigma_{ij_k}^{(\ell)}|$ is the absolute largest entry in the stress tensor for a given material point.

The adjoint system in Eq. (16) for the Lagrange multipliers $\boldsymbol{\lambda}^{(\ell)}$ is per load case ℓ, but the adjoint sensitivities in Eq. (15) sums the contributions of the Lagrange multipliers $\boldsymbol{\lambda}^{(\ell)}$ over all load cases L which is caused by the multiaxial stress states determined using superposition of the stresses for the fatigue load histories.

5 Numerical implementation

The numerical implementation for the optimization workflow is shown in Fig. 4 for the fatigue reserve factor analysis is shown in Fig. 2. The optimization is based on mathematical programming implemented in the software `Tosca Structure` (Dassault 2022). The fatigue analysis is performed using `fe-safe` (Dassault 2022a) and the finite element analysis and the corresponding adjoint sensitivities are obtained using `Abaqus/Standard` (Dassault 2022b). A 0.1% perturbation of the maximum absolute stress tensor entry for all present examples yield accurate approximations for the computation of the partial finite differences $\frac{\Delta F_k}{\Delta \sigma_{ij_k}^{(\ell)}}$ for each load case. Once the Lagrange multipliers $\boldsymbol{\lambda}^{(\ell)}$ are computed for each load cases, then, the total adjoint sensitivities $\frac{\mathrm{d}F}{\mathrm{d}\varphi}$ are obtained by summing over all load cases. The design variables are updated using the method of moving asymptotes (MMA) (Svanberg 1987, 2002, 2007) employing the calculated adjoint sensitivities.

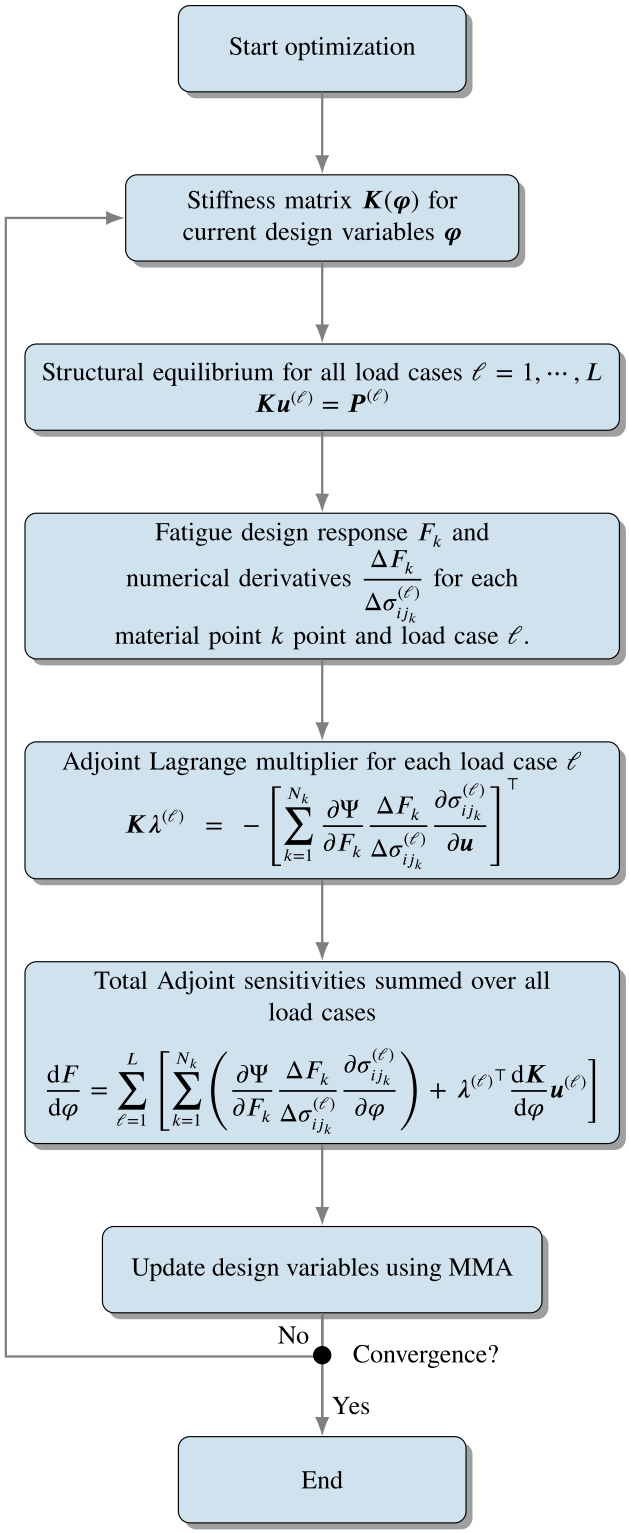

Fig. 4 Fatigue reserve factor (*FRF*) topology optimization workflow using numerical partial derivatives for the semi-analytical adjoint sensitivity calculation for $F = 1/FRF$ being aggregated over the material points k

If the design solution is not converged then the optimization workflow is repeated using the updated design variables. Two criteria must be fulfilled for obtaining optimization convergence. First, the relative change of the objective function must be below 0.1%. Secondly, the relative average change of the design variables must be below 0.5% between two subsequent optimization iterations.

6 Numerical examples

To demonstrate the proposed method three different models are considered. First, the L-bracket example from Zhang et al. (2019) is considered for three load cases

Table 1 Material parameters for both the L-Bracket and the aircraft bracket example

Parameter	Value
Young's modulus E	203 GPa
Poisson ratio ν	0.33
Ultimate tensile stress σ_u	400 MPa
Fully reversed fatigue limit σ_{-1}	188.3 MPa

where the compliance is minimized subject to a *FRF* constraint or a set of stress constraints. Secondly, an aircraft bracket having four load cases subject to a *FRF* constraint is also demonstrated to show that the proposed approach also works for a 3D application and various *FRF* parameter types. Finally, we present the optimization of a steering knuckle. In this example, the mass is minimized subject to several constraints for various nodal displacements and a strength constraint being either the von Mises stress or the *FRF*.

6.1 L-bracket having three load cases

The L-bracket example given in Zhang et al. (2019) is applied as a reference benchmark example consisting of 2D plane stress continuum elements [CPS4 (Dassault 2022b)]. The elements have an edge length of 1.0 mm yielding 25,600 finite elements. The material parameters are given in Table 1. The filter radius in Eq. (3) for the design variable filter is set to 1.6 mm. The applied load histories are shown in Fig. 5. The *FRF* strength optimization problem is defined as

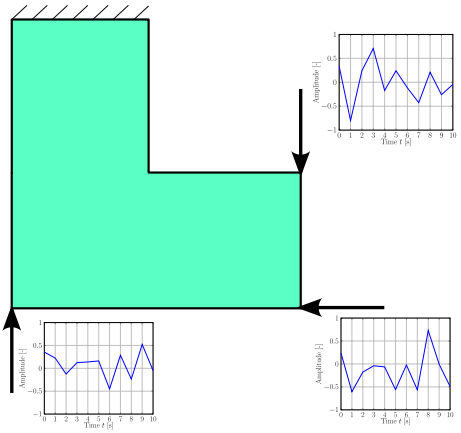

Fig. 5 L-bracket subject to three loads and corresponding load histories

$$\mathbb{P} = \begin{cases} \min & \sum_{\ell=1}^{L=3} c^{(\ell)} \\ \text{s.t.} & \dfrac{V}{V_0} \le 0.3 \\ & F = \dfrac{1}{FRF} \le 1.0 \end{cases} . \tag{18}$$

The index ℓ refers to the three load cases shown in Fig. 5. The sum of compliance for the three load cases are minimized subject to a relative volume constraint of 30% and a F constraint ensuring the *FRF* to be larger than one for all material points. The prismatic hull is considered as *FRF* parameter in (18) (Mamiya et al. 2009).

Furthermore, two additional stress strength optimizations are performed using a stress constraint at each load history point t_i, where $i \in \{0,, 1, \dots, 10\}$, see Fig. 5. Then the two stress strength topology optimization formulations are defined as

$$\mathbb{P}_{\sigma_{\text{Mises}}} = \begin{cases} \min & \sum_{\ell=1}^{L=3} c^{(\ell)} \\ \text{s.t.} & \dfrac{V}{V_0} \le 0.3 \\ & \sigma_{\text{Mises,t}_i} \le 188.3\,\text{MPa} \end{cases} \tag{19}$$

and

$$\mathbb{P}_{\sigma_1} = \begin{cases} \min & \sum_{\ell=1}^{L=3} c^{(\ell)} \\ \text{s.t.} & \dfrac{V}{V_0} \le 0.3 \\ & \sigma_{1,t_i} \le 188.3\,\text{MPa} \end{cases} , \tag{20}$$

where σ_{Mises} is the von Mises stress and σ_1 is the maximum principal stress, respectively.

The optimization results of the different optimization formulations are shown in Table 2. The different optimized density distributions as well as the *FRF* postprocessing results are shown together with the corresponding convergence

optimization history for each optimization formulation. The strictly compliance optimized design having no strength constraint has the *FRF* hotspot at the sharp retained corner due to the expected stress singularity at the predefined corner. All the other optimized designs, having strength constraints, do not have a sharp corner in order to fulfill the *FRF* requirement or the stress requirements. Note that the principal stress constraint design has some remaining intermediate densities in the final optimized design. Furthermore, the optimization iteration history for the principal stress constraints oscillate quite a lot for the first 60 optimization iterations, while the optimization formulation for the *FRF* constraint converges smoothly to the constraint value. The optimization iteration history for the von Mises stress constraint formulation also slightly oscillates until optimization iteration 40 but has rather smooth converge for the last optimization iteration.

The constraint values are compared in a crossover validation in Table 3 to show the impact of the strength formulation on the performance of the different designs. The strictly compliance optimized design yields the stiffest design for the objective function while the other strength constrained optimization formulations lead to designs having lower stiffness. The *FRF*-constrained optimization leads to the stiffest design among the three strength optimized designs. The strictly compliance optimized design and the principal stress σ_1 constrained design both have *FRF* causing fatigue failure as *FRF* is less than one, whereas the design for the von Mises σ_{Mises}-constrained optimization leads to a design having *FRF* being larger than one but with a compliance being higher than the compliance of the design optimized using a *FRF* constraint. Consequently, a stress strength optimized design would either fail for fatigue or have a too low a stiffness.

6.2 Aircraft bracket

In this section, we apply *FRF* topology optimization to the aircraft bracket as shown in Steltner et al. (2023). The model is subject to four load cases at the same loading point but having different load histories. All optimizations are performed using different *FRF*s parameter types to investigate the influence of the chosen *FRF* parameter type on the optimized designs and the corresponding optimization convergence. The bracket is shown in Fig. 6. The model is discretized using 448,914 first-order linear tetrahedral continuum elements having an average edge length of 2.16 mm (C3D4 (Dassault 2022b)). The subdomains around the holes for the loading point and the boundary conditions are excluded from the design domain. The load at the center of the top hole is applied using a distributed coupling formulation transmitting the forces from the loading point to the specified coupling nodes, see (Dassault 2022b). A force acting in the z-direction is given as $F_z = \pm 11.27$ kN for the first two load cases. A force acting only in the x-direction is defined to be $F_z = \pm 6.44$ kN for the other two load cases.

The filter radius in (3) for the design variable filter is set to 5.4 mm. Two different optimizations are tested in this example:

1. Minimizing the maximum compliance subject to a volume constraint and a *FRF* constraint.
2. The material volume as objective function to be minimized subject to compliance constraints and a *FRF* constraint.

Crossover checks are done for each of the two optimization formulations by applying the different *FRF* parameter types on validation models where the validation models are generated from extracted surfaces using an iso-cut value of 0.3 for the optimized density distribution of the bracket.

6.2.1 Minimizing compliance

Minimizing the compliance is a typical objective function for an industrial topology optimization application.

In this example, we show the same optimization as in the previous section can be done for 3D industrial optimization applications using various *FRF* parameter types.

The optimization target is to minimize the maximum compliance over all four load cases. Additionally, we specify the volume fraction to be below 20% and the *FRF* value should be above 1.2. Hence, the optimization formulation can be summarized as

$$\mathbb{P} = \begin{cases} \min \ \max C^{(\ell)} \\ \text{s.t.} \ \ \boldsymbol{K}\boldsymbol{u}^{(\ell)} = \boldsymbol{P}^{(\ell)} \\ \quad \dfrac{V}{V_0} \leq 0.2 \\ \quad \dfrac{1}{FRF} \leq \frac{1}{1.2} \end{cases} . \tag{21}$$

Here, $\ell \in [1, 2, 3, 4]$ defines the number for the given load case. The MIN-MAX formulation for the compliance over the load cases applied in Eq. (21) is solved as a standard optimization problem in which the objective function is remodeled into a set of constraints using the bound formulation (Taylor and Bendsøe 1984; Olhoff 1989).

The optimized designs are shown in Table 5. The convergence plots for the optimization iteration history shows that the *FRF* constraint as well as the volume constraint are both active and feasible for the last optimization iterations. The optimization converges after less than 70 optimization iterations for all *FRF* parameter types.

The validation run on the smoothed geometries shows that the most critical regimes are the sharp corners around the eight holes for the boundary conditions and the hole for

Table 2 Optimized designs for the L-bracket subject to three load cases applying different optimization formulations

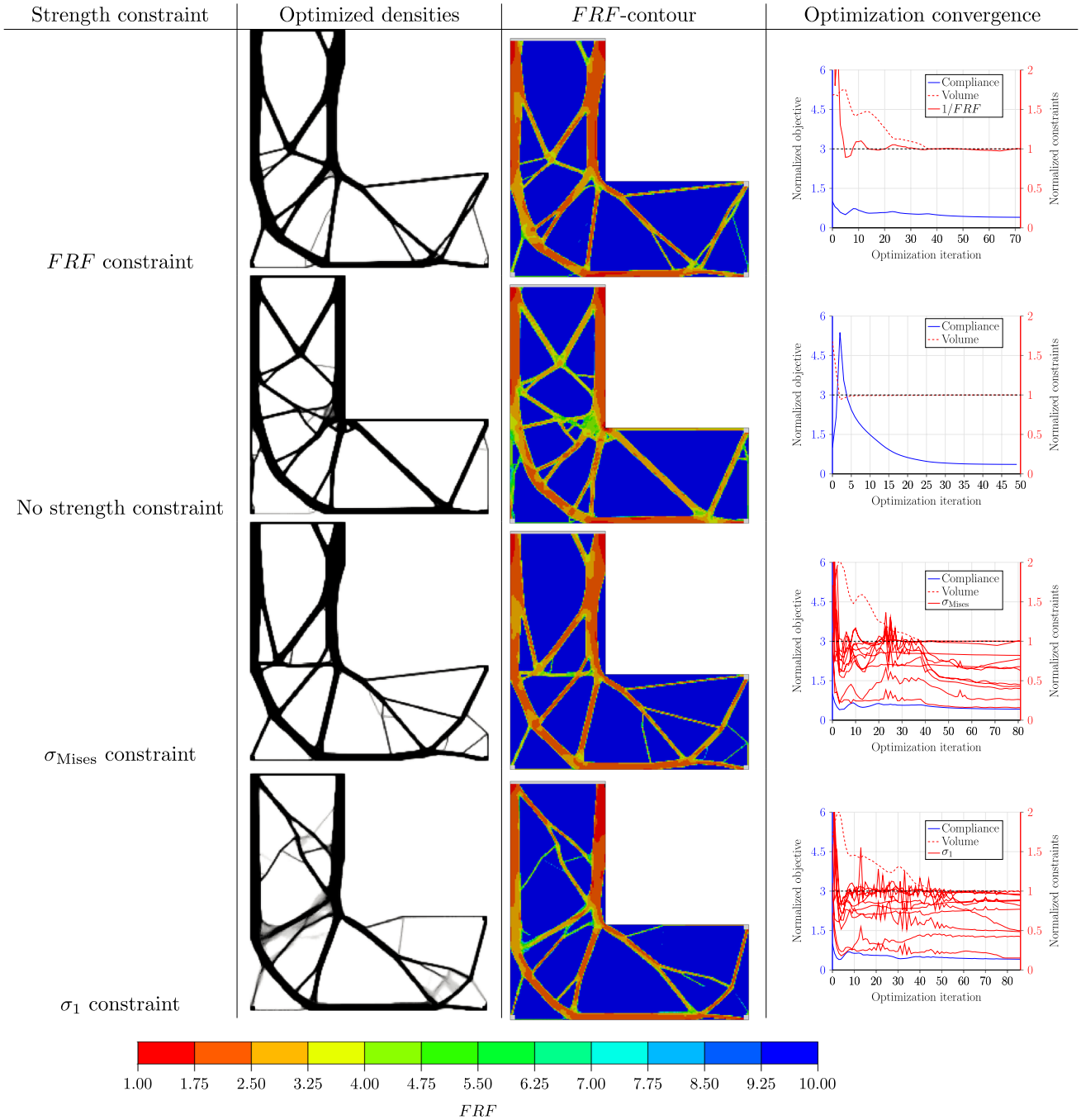

The compliance is the objective function minimized for all four optimization formulations subject to a relative volume constraint of 30%. Three of the optimized designs have a strength constraint being either the fatigue reserve factor (*FRF*), the von Mises stress or the maximum principle stress

the loading point. Additionally, the optimizations applying Brown-Miller, Prismatic Hull, and Dang Van as *FRF* parameter type show that not only the boundary condition and loading regions are critical for failure but also other parts of the component are likely to reach the endurance limit.

Table 4 shows the crossover check for the optimized designs. Therefore, each row corresponds to the *FRF* parameter type applied for the optimization while each column shows the method applied for crossover evaluation. It can be seen that the normal stress criterion tends to be the most conservative method among the applied *FRF* parameter types. Ideally, the highlighted cells should be close to the

Table 3 Crossover validation of the optimized designs in Table 2

Strength constraint	Compliance	*FRF*	Max σ_{Mises}	Max σ_1
$FRF \geq 1.0$	1912	1.00	205	174
No constraint	1723	0.53	397	353
$\sigma_{\text{Mises}} \leq 188.3$	2004	1.04	190	177
$\sigma_1 \leq 188.3$	1966	0.95	224	185

The row indicates which strength constraint is used for the optimization while the column provides the evaluated structural responses

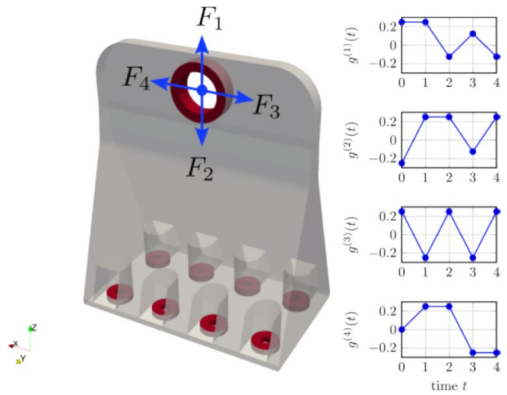

Fig. 6 Aircraft bracket and the applied load histories. The red marked subdomains are excluded from the design domain for the topology optimization

constraint value of 1.2. However, this is not always the case for the smoothed designs and corresponding *FRF* post-processing results. Still, the designs for all *FRF* constraints except from the design for the Brown-Miller *FRF* constraint have *FRF* values at least above 1.0, i.e., the designs are safe against fatigue failure being below the endurance limit.

6.2.2 Minimizing volume

In contrast to the previous optimization formulation in Sect. 6.2.1, we now change the objective function to minimize the material volume, and hence, the mass of the structure is minimized. To obtain a well-defined optimization formulation, we introduce compliance constraints for all four load cases. Due to symmetry and linear structural modeling then the first pair and the last pair of load cases have the same compliance value. The additional *FRF* constraint should be above 1.25. Hence, the optimization formulation reads

$$\mathbb{P} = \begin{cases} \min\ V(\boldsymbol{\varphi}) \\ \text{s.t.}\ \ \boldsymbol{K}\boldsymbol{u}^{(\ell)} = \boldsymbol{P}^{(\ell)} \\ \qquad \boldsymbol{u}^{(\ell)\top}\boldsymbol{P}^{(\ell)} \leq 1000\ \text{Nmm} \cdot \\ \qquad \dfrac{1}{FRF} \leq \dfrac{1}{1.25}. \end{cases} \tag{22}$$

Again, ℓ defines the four considered load cases. The optimized designs, the validation model, and the optimization convergence history are shown in Table 6. The optimization iteration history shows that both the compliance and the *FRF* constraints are active and feasible for all *FRF* parameter constraint types. Furthermore, all optimization convergences are rather smooth, while the number of optimization iterations remains below 60 optimization iterations independent upon the applied *FRF* parameter type.

Even though the volume fraction is around 20% for all optimized designs, the optimized designs look quite different for each *FRF* parameter type. While the optimizations considering Normal Stress and Normal Strain as parameter type for *FRF*s cause rather bulky designs then the other optimized designs are more truss-like structures.

Similar to the previous optimization then the smoothed designs share in common that the smallest *FRF* values appear at the sharp corners close to the holes for the boundary conditions. However, due to the low volume fraction, especially, the optimized designs for Prismatic Hull and Dang Van *FRF* contain small members. However, these members are not always realistic for industrial applications as they would fail quite early caused by high static stresses. Therefore, minor members are removed during the smoothing procedure for obtaining a more realistic estimate of the *FRF* values.

The crossover check considering the smoothed models are shown in Table 7. All highlighted diagonal cells except for the Dang Van case have *FRF* values being greater or equal to one. However, the smoothed design

Table 4 Crossover check of the different *FRF* parameter types for the smoothed topology-optimized designs of the aircraft bracket shown in Table 5 for minimizing maximum compliance subject to a volume constraint of 20% and a *FRF* constraint of 1.2

Evaluation of *FRF* for different parameter types					
	Normal stress	Normal strain	Brown-Miller	Prismatic Hull	Dang Van
Optimization constraint *FRF* parameter type					
Normal stress	**1.02**	1.31	1.24	1.34	1.14
Normal strain	0.99	**1.30**	1.19	1.28	1.10
Brown-Miller	0.83	1.02	**0.92**	0.95	2.31
Prismatic Hull	0.80	1.07	0.99	**1.10**	2.23
Dang Van	0.93	1.25	1.15	1.24	**1.15**

Table 5 Optimized density distributions for different *FRF* parameter types, the corresponding smoothed designs, and *FRF* calculated for the smoothed designs

FRF parameter constraint	Optimized density distribution	Smoothed design	*FRF* evaluation	Optimization convergence
Normal Stress	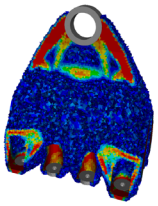	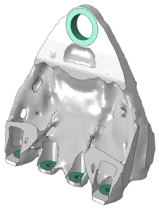	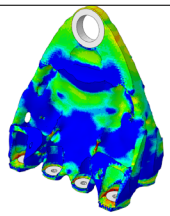	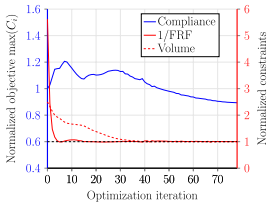
Normal Strain	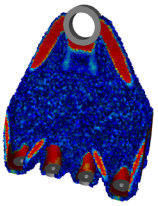	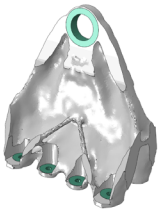	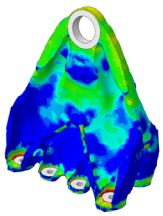	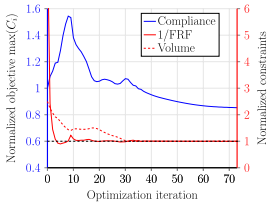
Brown-Miller	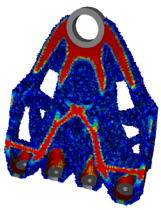	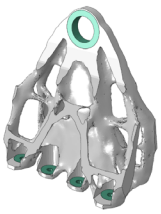	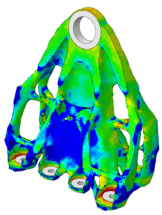	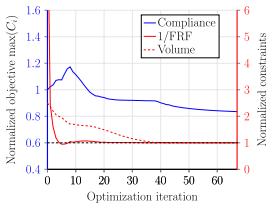
Prismatic-Hull	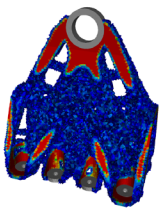	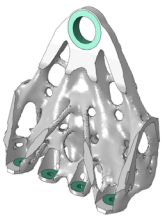	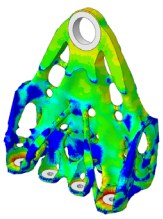	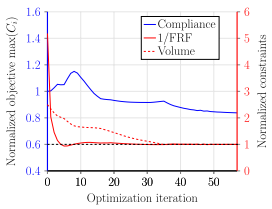
Dang-Van	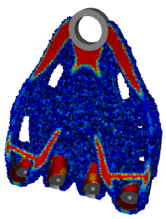	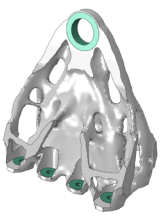	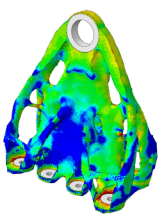	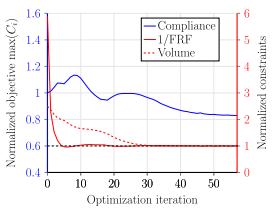

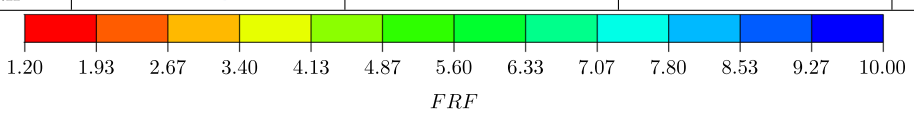

Optimization convergence for compliance minimization subject to volume constraint of 20% and a *FRF* constraint of 1.2

Table 6 Crossover check of the different *FRF* parameter types for the smoothed topology-optimized designs of the aircraft bracket shown in Table 7 for minimizing volume subject to compliance constraints and a *FRF* constraint of 1.25

Evaluation of *FRF* for different parameter types					
	Normal stress	Normal strain	Brown-Miller	Prismatic Hull	Dang Van
Optimization constraint *FRF* parameter type					
Normal stress	**1.34**	1.83	1.66	1.65	1.31
Normal strain	1.20	**1.63**	1.56	1.68	1.31
Brown-Miller	1.03	1.49	**1.46**	1.51	1.10
Prismatic Hull	0.97	1.10	1.01	**1.00**	0.65
Dang Van	0.50	0.52	0.46	0.55	**0.54**

considering Dang Van stay far below the given constraint. This may indicate that the member size should be further constrained for future optimizations, for instance using the approach from Carstensen and Guest (2018).

6.3 Steering Knuckle

In the following example, we compare static strength optimization with the fatigue topology optimization. The model as well as the load histories for the fatigue analysis are shown in Fig. 7. The model consists of 258,506 C3D4 elements with an average edge length of 2.02×10^{-3} mm. The model is clamped in the center while four static load cases are applied to the points where loads are introduced. The loads are applied in the 3D model at different locations having different directions and amplitudes, respectively. Hence, the stresses driving the fatigue damage optimization are highly multiaxial and non-proportional in space and time. The applied forces and moments are given in Table 9. The material parameters are given in Table 8. For the static stress strength optimization, a constraint on the maximum von Mises stress is defined, while in the fatigue optimization the *FRF* is limited to 1.0. In this case, the Brown-Miller damage type is applied for the *FRF* calculation. Hence, the two optimization formulations read

$$\mathbb{P}_{\text{static}} = \begin{cases} \min_{\boldsymbol{\varphi}} \; V(\boldsymbol{\varphi}) \\ \text{s.t.} \quad \boldsymbol{K}\boldsymbol{u}^{(\ell)} = \boldsymbol{P}^{(\ell)} \\ \qquad \sigma_{\text{vM}}^{(\ell)} \leq 250\,\text{MPa} \\ \qquad d_i \leq 0.12\,\text{mm} \end{cases} \tag{23}$$

and

$$\mathbb{P}_{FRF} = \begin{cases} \min_{\boldsymbol{\varphi}} \; V(\boldsymbol{\varphi}) \\ \text{s.t.} \quad \boldsymbol{K}\boldsymbol{u}^{(\ell)} = \boldsymbol{P}^{(\ell)} \\ \qquad \dfrac{1}{FRF} \leq 1.0 \\ \qquad d_i \leq 0.12\,\text{mm} \end{cases} \tag{24}$$

The filter radius for the design variable filter is set to 3.23 $\times10^{-3}$ mm.

The density distribution of the optimized designs are shown in Fig. 8, the contour plots of the optimized designs are shown in Table 10 and the optimization iteration history is shown in Fig. 9. Therefore, the optimized designs have a volume fraction of 5.7 and 6.2% for the static strength and the *FRF* optimization, respectively. After applying an iso-cut smoothing of 0.3, the smoothed designs for validation have a volume fraction of 7.4 and 8.4%, respectively. The optimization convergence for both designs show that some of the displacement constraints are also active. Additionally, the strength and fatigue criteria are active for both designs. The optimization iteration history of *FRF* tends to oscillate in the initial and intermediate iterations. This is caused by the change of the *FRF* hotspot during the optimization iterations. Nevertheless, the optimized design fulfills both the *FRF* and the displacement constraints in the last optimization iterations. The bold marked diagonal numbers indicate when the parameter type for the *FRF* constraint in the optimization is also the parameter type for the *FR*F evaluation of the smoothed topology optimized design.

Furthermore, the validations in Table 10 show that the *FRF* is far below one for the static stress-optimized design and would fail from a fatigue point of view, while the *FRF* is almost one for the fatigue-optimized design and would not fail from a fatigue point of view.

7 Conclusion

We present a new approach for infinite fatigue life topology optimization based upon the inverse fatigue reserve factor (*FRF*) applied either in the objective function or as constraint. The present approach has the following advantages:

- Semi-analytical fatigue sensitivities are implemented for the fatigue reserve factor (*FRF*). Therefore, the fatigue optimization is not limited to a single or few *FRF* param-

Table 7 Optimized density distributions for different *FRF* parameter types, the corresponding smoothed designs, and *FRF* calculated for the smoothed designs

FRF parameter constraint	Optimized density distribution	Smoothed design	*FRF* evaluation	Optimization convergence
Normal Stress		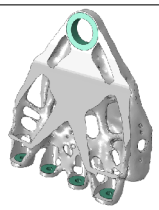	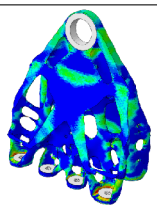	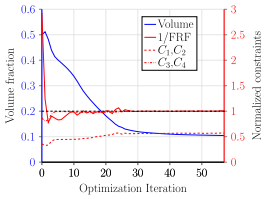
Normal Strain		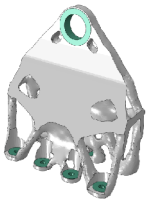	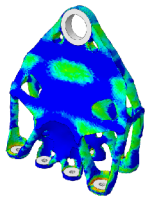	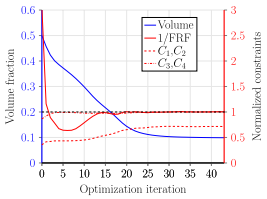
Brown-Miller		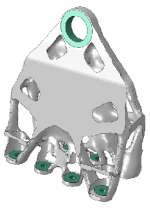	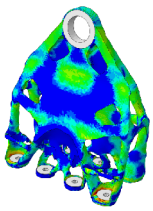	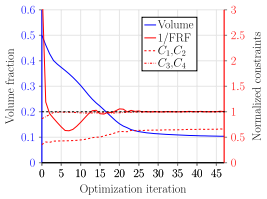
Prismatic-Hull	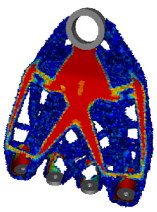	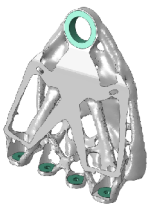	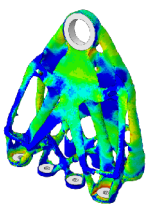	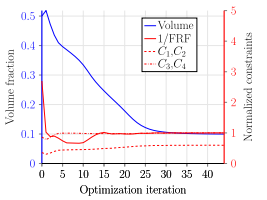
Dang Van	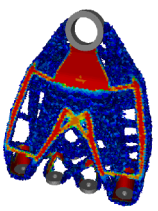	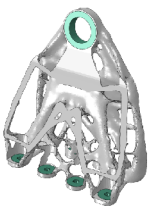	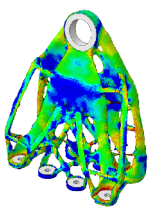	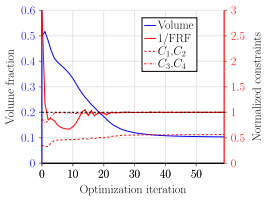

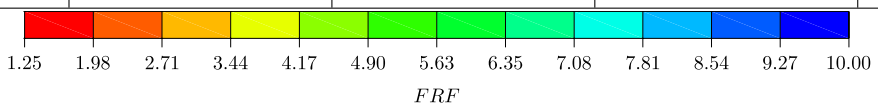

Optimization convergence for volume minimization subject to four compliance constraints and a *FRF* constraint of 1.25

Table 8 Material parameters for steering knuckle example

Parameter	Value
Young's modulus E	121.5 GPa
Poisson ratio ν	0.33
Ultimate tensile stress σ_u	845 MPa
Fully reversed cycle fatigue limit σ_{-1}	486 MPa

eter types and both rainflow counting and critical plane are supported. Thus, an arbitrary *FRF* parameter type can be optimized using adjoint sensitivities as long as the *FRF* only depends on the stresses. This approach is attractive for industrial applications where different *FRF* are applied for different material applications. Additionally, the semi-analytical fatigue sensitivity calculation

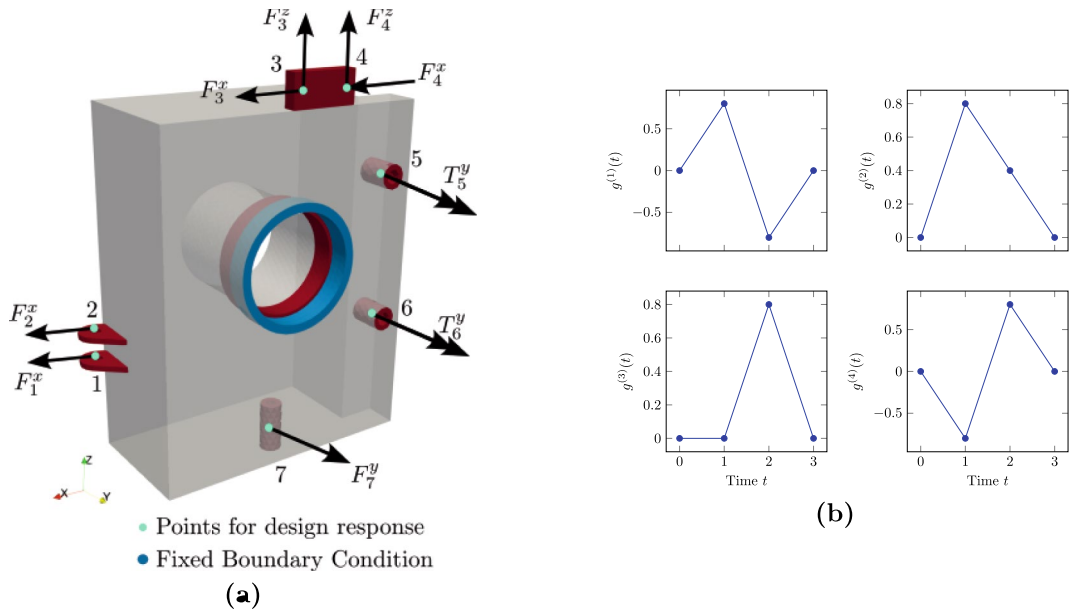

Fig. 7 **a** Design domain showing the boundary conditions for the four load cases having loading for different directions at different locations. **b** Load histories for the four load cases for the *FRF* calculation

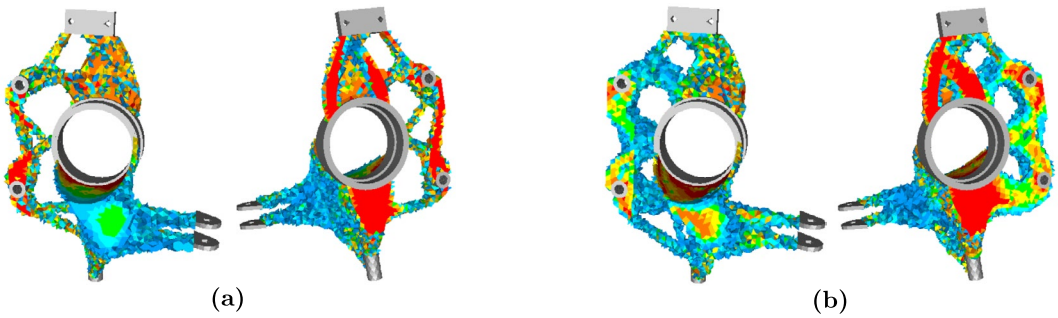

Fig. 8 Optimized density distributions for mass minimization subject to **a** a static stress strength constraint and **b** a *FRF* constraint, respectively

Table 9 Loads applied for each load case at the specified locations shown in Fig. 7a

	F_1^x	F_2^x	F_3^z	F_3^x	F_4^z	F_4^x	T_5^y	T_6^y	F_7^y
LC1	2170	2170	−2500	3860	−2500	3860	250	250	−2000
LC2	−85	−85	−50	230	−50	230	0	0	220
LC3	405	405	140	2565	140	2565	0	0	−5725
LC4	−425	−425	390	20	390	20	−250	−250	−300

is computational efficient as the finite difference for the partial derivatives of *FRF* with respect to the stresses is computed independently per material point.

- Several numerical examples of practical applications are shown for different *FRF* types. The influence of the different *FRF* types on the optimized designs show that the different *FRF* types yield very different optimized structural layouts. Additionally, several crossover checks for the different *FRF* types are presented showing significant variations in the *FRF* values.
- Well-posed optimization formulations are demonstrated having the fatigue reserve factor (*FRF*) present either in the objective function or as a constraint. Additionally, stiffness and mass requirements are introduced. Therefore, the numerical results show clear solid and void topology-optimized designs. This is also numerical verified through verification models reconstructed using

Table 10 Fatigue reserve factor evaluation of the smoothed topology optimization results using an iso-cut value of 0.3

View	Isometric	Front	Rear
Static strength FRF = 0.53	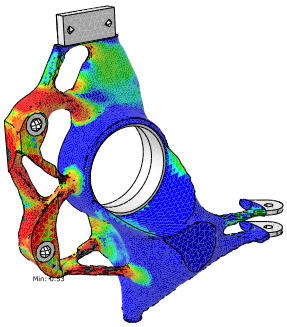	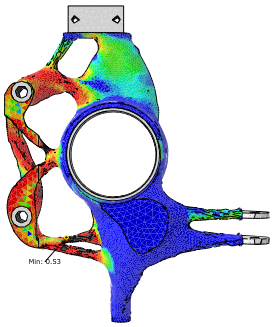	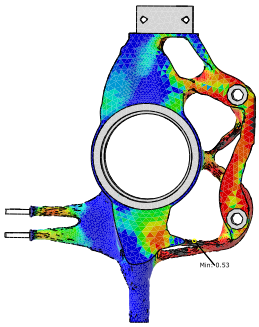
Fatigue reserve factor FRF = 0.98	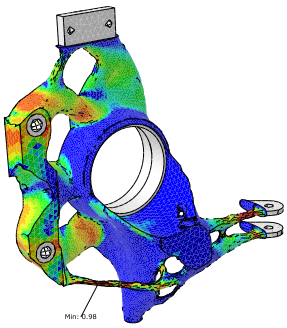	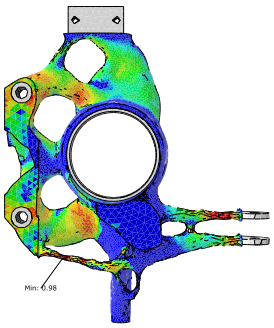	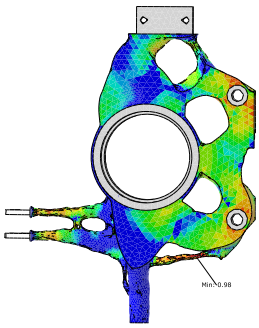

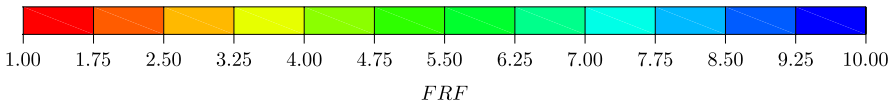

The static stress strength constrained optimized design has only half of the *FRF* compared to the design subject to fatigue constraint of 1.0. Some regions of the topology optimized design are similar due to the common stiffness requirements

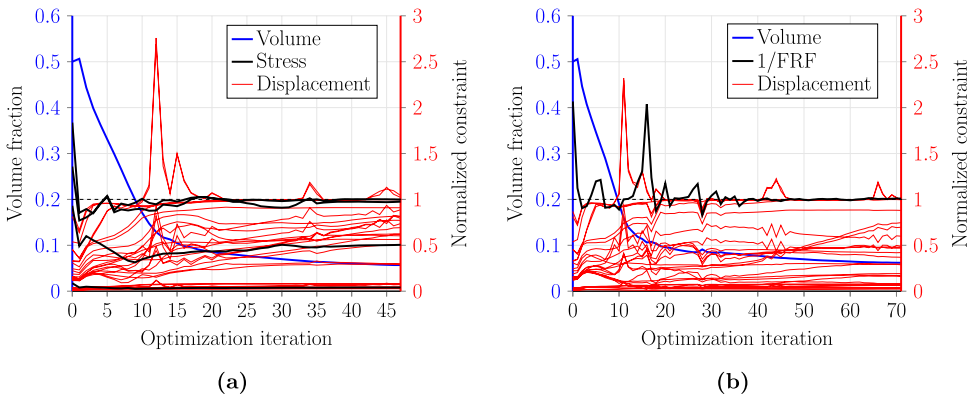

Fig. 9 Optimization iteration histories for the mass minimization subject to **a** a static stress constraint and **b** a *FRF* constraint, respectively

the smooth designs of the topology-optimized density distributions having *FRF* results being rather close to the *FRF* values observed directly for the topology-optimized density distributions.

- One of most important observations for the present fatigue topology optimization using *FRF* is that the number of optimization iterations is considerably reduced compared to the common literature for fatigue topology optimization as the present approach allows practical move limits for the design variables yielding a consistent optimization convergence. Traditionally, common literature for fatigue topology optimization applies heu-

ristic scaling of the fatigue values as well as low move limits for the design variables to suppress the highly non-linear coupling between the fatigue damages and the design variables. Since we use the inverse *FRF* instead of the fatigue damage then the fatigue design measure representing the damage scales almost linearly with the stresses and thereby, almost scales linear with respect to the design variables.

On the other hand, the major restriction of using the present infinite life fatigue topology optimization approach based upon *FRF* is that the optimization approach cannot address finite life fatigue optimization applications. For addressing finite life in topology optimization then the damage often has to be accumulated over time for all cycles. Therefore, the finite life fatigue response is typically a highly non-linear function of the stresses and no efficient finite life fatigue topology optimization approach can be defined using a safety factor addressing finite life fatigue having the same numerical advantages as the present *FRF* for finite life fatigue topology optimization applications and at the same time considering fatigue standards, including different parameter types, rainflow counting, and critical plane. Consequently, this has to be addressed in future work for finite life topology optimization.

Acknowledgements No funding was received for conducting this study.

Author Contributions RS contributed to Conceptualization, Methodology, Software, Writing—original draft preparation, and Writing—review and editing. BK contributed to Conceptualization, Methodology, and Writing—review and editing. DH contributed to Conceptualization, Methodology, and Writing—review and editing. CBWP contributed to Conceptualization, Methodology, Software, and Writing—review and editing.

Funding Open Access funding enabled and organized by Projekt DEAL.

Data availability The data that support the findings of this study are available from the corresponding author upon reasonable request.

Declarations

Conflict of interest The authors declare that they have no conflict of interest.

References

ASTM E1049-85 (2017) Standard practices for cycle counting in fatigue analysis. https://www.astm.org/e1049-85r17.html

Bendsøe MP, Sigmund O (2007) Topology optimization. World Scientific, pp 161–194

Bruggi M (2008) On an alternative approach to stress constraints relaxation in topology optimization. Struct Multidisc Optim 36(2):125–141. https://doi.org/10.1007/s00158-007-0203-6

Carstensen JV, Guest JK (2018) Projection-based two-phase minimum and maximum length scale control in topology optimization. Struct Multidisc Optim 58(5):1845–1860. https://doi.org/10.1007/s00158-018-2066-4

Dassault Systèmes (2022) Abaqus 2022 reference manual https://www.3ds.com/products/simulia/abaqus

Dassault Systèmes (2022) fe-safe 2022 reference manual https://www.3ds.com/products/simulia/fe-safe

Dassault Systèmes (2022) Tosca structure 2022 reference manual https://www.3ds.com/products/simulia/tosca

Holmberg E, Torstenfelt B, Klarbring A (2013) Stress constrained topology optimization. Struct Multidisc Optim 48(1):33–47. https://doi.org/10.1007/s00158-012-0880-7

Jeong SH, Choi D-H, Yoon GH (2015) Fatigue and static failure considerations using a topology optimization method. Appl Math Model 39(3):1137–1162. https://doi.org/10.1016/j.apm.2014.07.020

Karolczuk A, Kluger K, Łagoda T (2016) A correction in the algorithm of fatigue life calculation based on the critical plane approach. Int J Fatigue 83:174–183. https://doi.org/10.1016/j.ijfatigue.2015.10.011

Le C, Norato J, Bruns T, Ha C, Tortorelli D (2010) Stress-based topology optimization for continua. Struct Multidisc Optim 41(4):605–620. https://doi.org/10.1007/s00158-009-0440-y

Lee Y-L, Barkey ME, Kang H-T (eds) (2012) Front matter. Butterworth-Heinemann, Boston. https://www.sciencedirect.com/science/article/pii/B9780123852045000136

Mamiya E, Araújo J, Castro F (2009) Prismatic hull: a new measure of shear stress amplitude in multiaxial high cycle fatigue. Int J Fatigue 31(7):1144–1153. https://doi.org/10.1016/j.ijfatigue.2008.12.010. https://www.sciencedirect.com/science/article/pii/S0142112308002892

Meggiolaro MA, Castro JT Pd, Wu H (2015). Invariant-based and critical-plane Rainflow approaches for fatigue life prediction under multiaxial variable amplitude loading. Proced Eng 101:69–76. https://doi.org/10.1016/j.proeng.2015.02.010. https://www.sciencedirect.com/science/article/pii/S1877705815006086

Norato JA, Smith HA, Deaton JD, Kolonay RM (2022) A maximum-rectifier-function approach to stress-constrained topology optimization. Struct Multidisc Optim 65(10):286. https://doi.org/10.1007/s00158-022-03357-z

Oest J, Lund E (2017) Topology optimization with finite-life fatigue constraints. Struct Multidisc Optim 56(5):1045–1059. https://doi.org/10.1007/s00158-017-1701-9

Olesen AM, Hermansen SM, Lund E (2021) Simultaneous optimization of topology and print orientation for transversely isotropic fatigue. Struct Multidisc Optim 64(3):1041–1062. https://doi.org/10.1007/s00158-021-02995-z

Olhoff N (1989) Optimal structural design via bound formulation and mathematical programming. In: Brebbia CA et al. (eds)

Discretization methods and structural optimization—procedures and applications, vol 42, pp 255–262. Springer, Berlin, Heidelberg
Rychlik I (1996) Simulation of load sequences from rainflow matrices: Markov method. Int J Fatigue 18(7):429–438. https://doi.org/10.1016/0142-1123(96)80001-Z
Sartorti R, Möcker T, Kriegesmann B, Pedersen CB (2023) On non-parametric fatigue optimization. Int J Numer Methods Eng 124(5):1168–1192. https://doi.org/10.1002/nme.7158
Sigmund O, Maute K (2013) Topology optimization approaches: a comparative review. Struct Multidisc Optim 48(6):1031–1055. https://doi.org/10.1007/s00158-013-0978-6
Slebioda M, Giele R, Langelaar M (2023) Topology optimization for infinite fatigue life of cyclic symmetric structures subjected to non-proportional loading. Comput Struct286:107113. https://doi.org/10.1016/j.compstruc.2023.107113. https://www.sciencedirect.com/science/article/pii/S0045794923001438
Socie D (2000) Multiaxial fatigue society of automotive engineers. Electronic Publications. Society of Automotive Engineers, Warrendale. Includes bibliographical references. Title from PDF title page. SAE Web Site. Accessed 15 Aug 2012
Steltner K, Pedersen CBW, Kriegesmann B (2023) Semi-intrusive approach for stiffness and strength topology optimization under uncertainty. Optim Eng 24(3):2181–2211. https://doi.org/10.1007/s11081-022-09770-z
Stephens RI, Fuchs HO (eds) (2001) Metal fatigue in engineering 2nd edn. A Wiley-Interscience Publication, Wiley, New York. Includes bibliographical references and index
Suresh S, Lindström SB, Thore C-J, Torstenfelt B, Klarbring A (2020) Topology optimization using a continuous-time high-cycle fatigue model. Struct Multidisc Optim 61(3):1011–1025. https://doi.org/10.1007/s00158-019-02400-w
Suresh S, Lindström SB, Thore C-J, Klarbring A (2021) Topology optimization for transversely isotropic materials with high-cycle fatigue as a constraint. Struct Multidisc Optim 63(1):161–172. https://doi.org/10.1007/s00158-020-02677-2
Suresh S, Lindström SB, Thore C-J, Klarbring A (2022) Acceleration of continuous-time, high-cycle fatigue constrained problems in topology optimization. Eur J Mech A Solids 96:104723. https://doi.org/10.1016/j.euromechsol.2022.104723
Suresh S, Lindström SB, Thore C-J, Klarbring A (2022) Acceleration of continuous-time, high-cycle fatigue constrained problems in topology optimization. Eur J Mech A Solids 96:104723. https://doi.org/10.1016/j.euromechsol.2022.104723
Svanberg K (1987) The method of moving asymptotes—a new method for structural optimization. Int J Numer Methods Eng 24(2):359–373. https://doi.org/10.1002/nme.1620240207
Svanberg K (2002) A class of globally convergent optimization methods based on conservative convex separable approximations. SIAM J Optim 12(2):555–573. https://doi.org/10.1137/S1052623499362822
Svanberg K (2007) Mma and gcmma-two methods for nonlinear optimization. 1:1–15
Taylor J, Bendsøe MP (1984) An interpretation for min-max structural design problems including a method for relaxing constraints. Int J Solids Struct 20(4):301–314. https://doi.org/10.1016/0020-7683(84)90041-6
Verbart A, Langelaar M, van Keulen F (2016) Damage approach: a new method for topology optimization with local stress constraints. Struct Multidisc Optim 53(5):1081–1098. https://doi.org/10.1007/s00158-015-1318-9
Zhang S, Le C, Gain AL, Norato JA (2019) Fatigue-based topology optimization with non-proportional loads. Comput Methods Appl Mech Eng 345:805–825. https://doi.org/10.1016/j.cma.2018.11.015
Zienkiewicz OC, Taylor RL (2005) The finite element method for solid and structural mechanics. Elsevier